Highly Efficient Electron-Selective Layer Free Perovskite Solar Cells by Constructing Effective p–n Heterojunction

Peng Cui, Dong Wei, Jun Ji, Dandan Song, Yaoyao Li, Xin Liu, Jing Huang, Tianyue Wang, Jingbi You, and Meicheng Li*

A heterojunction concept with an n-type self-doped perovskite and a p-type hole-transport material was proposed for fabricating highly efficient electron-selective layer (ESL)-free perovskite solar cells (PSCs). The self-doping property of the perovskite is controlled by defects engineering, which can change from p- to n-type, and the n-type self-doping degree is tuned serially by precursor composition and process conditions. Meanwhile, the compact homogenous and large-grain film morphology is achieved by introducing mixed nonpolar aprotic solvents to obtain optimal balancing between densification and grain size. Hence, the ESL-free PSCs with n-type self-doped compact $CH_3NH_3PbI_3$ film exhibit state of the art performance with the highest efficiency of 15.69%. Besides, the as-fabricated ESL-free PSCs, which keep their initial efficiencies for a period of 21 days without degradation, demonstrate better long-term stability compared to the conventional planar PSCs.

Introduction: Organometallic lead halide perovskite materials (such as $CH_3NH_3PbI_3$) are a promising class of light absorbers for highly efficient and low-cost solar cells. The perovskite solar cells (PSCs) utilizing this kind of perovskites have made impressive strides in power conversion efficiency (PCE) from 3.8 to 22.1% within the last 6 years.[1–6] The PSCs are considered to work on the p–i–n junction[7–8] with the two typical architectures including the mesoscopic architecture and the planar architecture. The mesoscopic PSC evolves from the solid state dye-sensitized solar cell, which is constructed by a fluorine doped tin oxide (FTO) electrode, an electron-selective layer (ESL, also called hole-blocking layer), a mesoporous TiO_2 or Al_2O_3 scaffold, a perovskite absorber, a hole-transport material (HTM), and a metal electrode, first reported by N. G. Park et al. in 2012.[9] Subsequently, it is proved that the mesoscopic scaffold is not necessary for PSCs to achieve high efficiency, i.e., a simple planar architecture incorporating vapor-deposited perovskite film as absorbing layer enables the solar-to-electrical PCE of the PSCs of over 15%.[10] To obtain efficient PSCs with simpler fabrication methods, further simplifying the device architecture is also possible, because perovskite possesses ambipolar carrier transport property, which can functionalize as carrier transport materials. In this context, HTM-free PSCs are achieved, which avoid the fabrication and the use of the expensive organic HTMs.[11–14]

Besides the HTM-free architecture, the ESL (usually using metal oxides, e.g., TiO_2, ZnO) is also not necessary for PSCs to realize the photovoltaic conversion.[15–18] The ESL-free PSCs avoid complex fabrication process of the ESLs, especially the multiple high-temperature treatment required for fabricating TiO_2 ESL, and have the high device stability potential (it is reported that TiO_2 induces the decomposition of the perovskite film by its oxygen vacancies[19]). However, the ESL-free PSCs possess relative low PCE compared to standard PSCs with full components. One plausible origin of the low performance of the ESL-free PSCs is the ineffective electron selection and the resultant carrier recombination at FTO/perovskite interface, due to the absence of the ESL. As the PSCs with complete architecture work on the p–i–n junction, the perovskite film acts as an i-type layer and yields no selectivity towards the carrier transport. Herein, in ESL-free PSCs, both electrons and holes can be transported to the FTO/perovskite interface and recombine there, leading to their low efficiency. Moreover, the rough and non-uniform perovskite film induced by the absence of the ESL will generate pinholes and cause severe recombination, resulting from the shunt paths between HTM and FTO, which is another cause for the low device efficiency of the ESL-free PSCs.

Therefore, to obtain highly efficient ESL-free PSCs, efficient carrier selection and compact homogeneous perovskite film are crucial. For efficient carrier selection, an asymmetrical p–n junction in PSCs is essential. In ESL-free PSCs, HTM can select holes and in consequence, the perovskite is desired to be n-type for efficient electron selection. Fortunately, it is proved that the perovskite can be self-doped to n- or p-type by defect engineering.[20–22] Thereby, the combination of n-type doped perovskite and HTM (e.g., spiro-MeOTAD) is possible to form the effective heterojunction for highly efficient ESL-free PSC.

M. Li, P. Cui, D. Wei, J. Ji, D. Song, Y. Li, X. Liu, J. Huang, T. Wang
State Key Laboratory of Alternate Electrical Power System with Renewable Energy Sources, School of Renewable Energy, North China Electric Power University, Beijing 102206, China
E-mail: mcli@ncepu.edu.cn
J. You
Institute of Semiconductors, Chinese Academy of Sciences, Beijing 100083, China
J. You
College of Materials Science and Opto-electronic Technology, University of Chinese Academy of Sciences, Beijing 100049, China

For compact homogeneous perovskite film, the key is to improve its deposition method. The perovskite film, deposited on the FTO by a typical two-step solution deposition method or the solvent vapor annealing method, is usually rough, uncompact, and porous with small-grains. Recently, the one-step solution deposition method employing consecutive non-polar aprotic solvent (NPAS) dripping was proposed for fabricating uniform perovskite films on ESL. The additional NPAS (e.g., diethyl ether,[23] toluene,[24] chlorobenzene,[25] etc.) is able to enhance the perovskite pore filling, increase the grain size up to microns and improve the uniformity of the film. From this viewpoint, the compact pinhole-free perovskite films for highly efficient ESL-free PSCs are also probably able to be obtained, utilizing the one-step solution deposition method by optimizing the consecutive NPAS dripping.

In this work, we report the realization of self-doped compact homogenous pure lead halide perovskite ($CH_3NH_3PbI_3$) film for highly efficient ESL-free PSCs by constructing an effective p–n heterojunction. The n-type perovskite is obtained by self-doping through a low-temperature annealing process (100–150 °C). The compact homogenous perovskite films were

deposited directly on to the FTO substrates by the modified one-step solution deposition method using mixed NPASs. The ESL-free PSCs exhibit the highest PCE of up to 15.69%, which also show a better long-term stability in ambient atmosphere compared to the conventional planar PSCs.

Results: A schematic illustration of the planar perovskite solar cells with diffident device architecture is depicted in **Figure 1**a–c. The typical architecture is based on a complete p–i–n heterojunction: the near-intrinsic perovskite film, which acts as a solar light absorber, is sandwiched between an ESL and an HTM. Nevertheless, in the ESL-free PSC, because of the lack of n-type TiO_2 compact only p–i junction exists, leading to an ineffective carrier selection and the resultant low PCE. For highly efficient ESL-free PSC, constructing an effective p–n heterojunction with n-type perovskite and p-type hole-transport material is crucial. The ability of perovskite to tune its optical and electronic properties enables a p–n heterojunction ESL-free PSC to enhance device efficiency.

The self-doping property of the perovskite films was adjusted by controlling the growth conditions. X-ray photoemission spectroscopy (XPS) was employed to verify the composition and
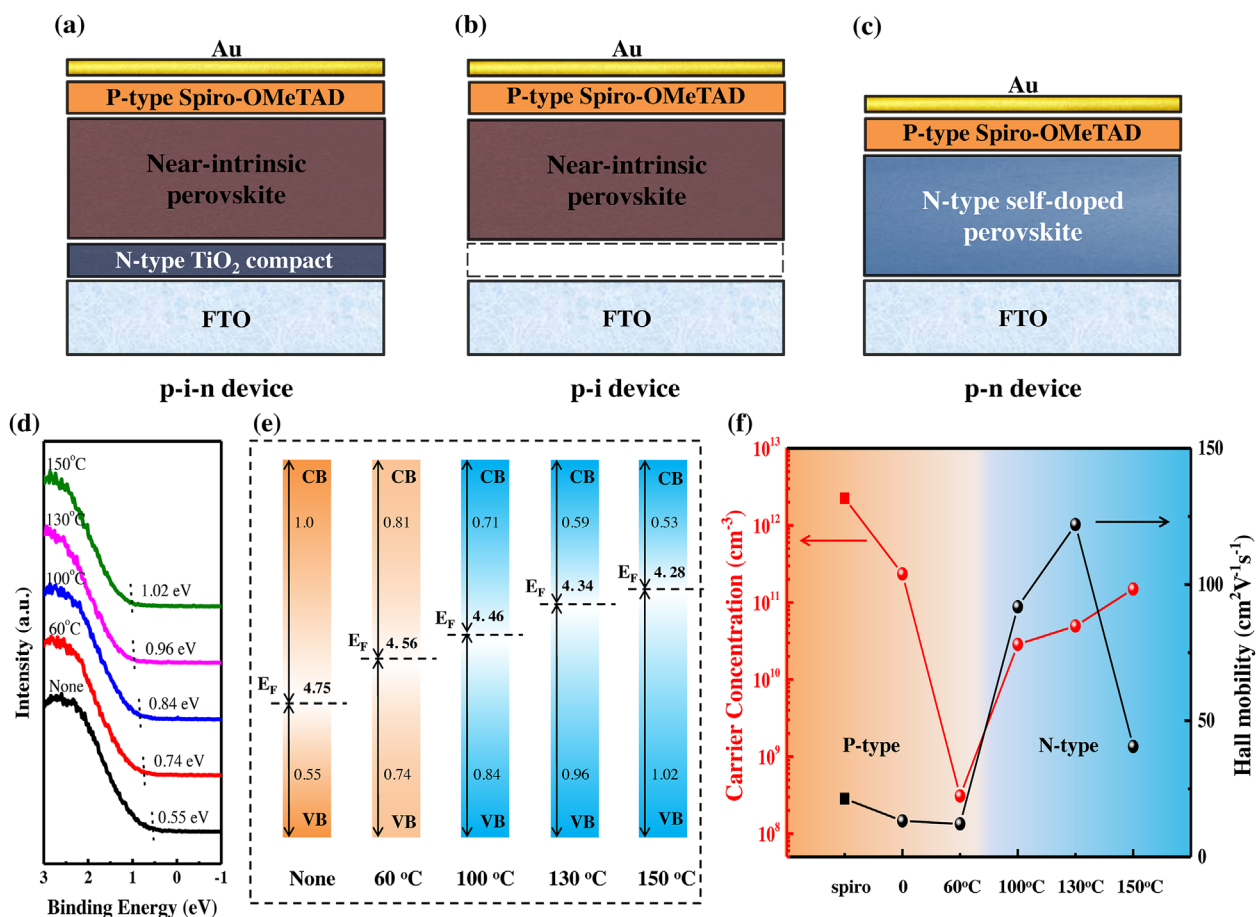

Figure 1. Schematic illustration of planar perovskite solar cells: (a) the conventional p–i–n device; (b) the p–i device without electron-selective layer; (c) the p–n device with n-type self-doped perovskite. (d) Valence spectra of $CH_3NH_3PbI_3$ films formed by one-step solution method with different annealing temperatures. (e) The energetic levels of the corresponding perovskite films. (E_F, CB, and VB represent Fermi level, conductive band and valence band, respectively; the column colors of orange and blue represent the p- and n-type, respectively.) (f) Annealing temperatures dependent carrier concentration (red) and carrier mobility (black) in perovskite films (circle) and the spiro-MeOTAD film (square) by Hall measurement.

ADVANCED
SCIENCE NEWS
www.advancedsciencenews.com

Solar RRL
www.solar-rrl.com

RAPID RESEARCH LETTER

the valence spectra of the perovskite films under different annealing temperatures. The valence spectra and the schematic energy level of the perovskite films are shown in Figure 1d and e. It can be seen that the energy difference between the valence band (VB) and the Fermi level (E_F) is 0.55 eV in the condition of the perovskite film without annealing, which reveals the p-type doping property of the as-prepared perovskite film considering its energy bandgap of 1.55 eV. With the increase of the annealing temperature, its E_F is shifted close to the conduction band (CB). For the perovskite film annealed at 100 °C, the energy difference between VB and E_F is 0.84 eV, which reveals its intrinsic, or lightly n-type doping property. By further increasing the annealing temperature to 150 °C, the E_F shifts up to the location of only 0.53 eV below the CB, resulting in an obviously n-type doped film.

Moreover, the doping feature of the perovskite films was also characterized by Hall effect measurement, which was performed with four contacts Hall bar method. Figure 1f and Supporting Information Table S1 show the mobility and carrier concentration measured by Hall effect of perovskite films fabricated by varied annealing temperature and the spiro-MeOTAD film. It can be seen that the doping type of perovskite films with low annealing temperature (none and 60 °C) is p-type. The perovskite film at 60 °C becomes closer to the intrinsic, as its carrier concentration decreases, compared to no annealing

perovskite film. Notably, increasing the annealing temperature to 100 °C converted the perovskite films from p-type to lightly n-type with an electron concentration of $2.861e+10\,cm^{-3}$. With the further increase of the annealing temperature, the electron concentration of perovskite films continues to increase. The reduced carrier mobility with the annealing temperature of 150 °C can be explained by the formation of PbI_2 in perovskite films (as revealed by the XRD patterns shown in **Figure 2**f), because the dopants always serve as charge carrier scattering centers. The doping feature of as-prepared perovskite films derives from the defects.[20–22] Pb vacancies and/or I interstitials are reduced, accompanied by the removing of excess CH_3NH_3I, leading to the doping feature from p-type moderating to n-type of the films. At high temperature (150 °C), the $CH_3NH_3^+$ is easier to remove, leading to a Pb-rich condition, and making the doping property of the perovskite film n-type. Hence, it is clear that the self-doped perovskite films with the self-doping property varied from weak p-type to n-type can be obtained by suitable treatments.

To confirm the p–n heterojunction and depletion field in the devices, the Kelvin probe force microscopy (KPFM)[7,28,29] has been used to map the contact area between the spiro and the perovskite layers (Supporting Information Figure S1). Figure S1b and c show an AFM topographic and the corresponding KPFM potential images, respectively. And the potential line
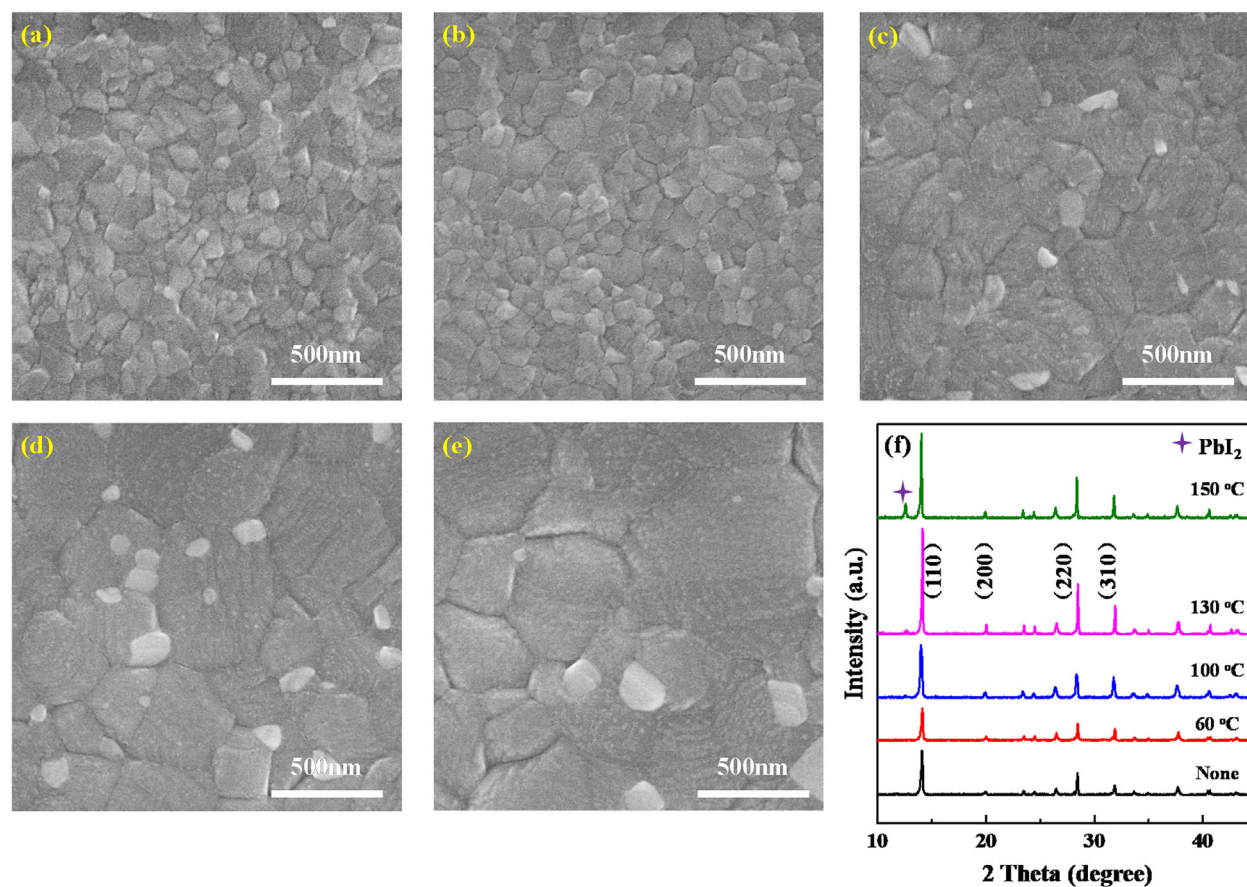
Figure 2. Scanning electron microscope (SEM) images of the $CH_3NH_3PbI_3$ films with different annealing temperatures of (a) none, (b) 60 °C, (c) 100 °C, (d) 130 °C, and (e) 150 °C. (f) Shows the XRD patterns of the FTO/$CH_3NH_3PbI_3$ films with different annealing temperatures.

Solar
RRL
www.solar-rrl.com

ADVANCED
SCIENCE NEWS
www.advancedsciencenews.com

profile in the Figure S1d is extracted from the white line position in the Figure S1c, which demonstrates the local contact potential difference (CPD) distribution between tip and sample across the spiro and perovskite layers. The granular morphology of the nominally 300–500-nm-thick perovskite can be clearly observed at the right of the image, which is consistent with the scanning electron microscope (SEM) result. Toward the left side, the spiro layer is smooth and flat. The internal interface appears as straight line in the contact area, indicating a sharp and well-defined interface between the materials. KPFM measure is thus sensitive to the surface work functions of the materials. Assuming that the tip work function remains constant during a line scan, the CPD reflects the built-in potential of the layers. From the potential results, the CPD from the spiro toward the perovskite first increases slowly and then declines rapidly at the interface, which reveals the continuous change of the electric field distribution with the p-type spiro and n-type perovskite. Thus, the CPS profile further confirms the p–n behavior at the spiro/perovskite interface.

The compact homogeneous and gain-size-suitable perovskite film is also critical for highly efficient ESL-free PSCs. Hence, the surface morphologies of as-prepared perovskite films were characterized. As shown in Figure 2a and b, the perovskite films without annealing, or annealed at low temperature (60 °C), are composed of diminutive, dense, and non-uniform grains. In contrast, compact and uniform perovskite films with large grain size are formed under a relatively high annealing temperature in their crystallization process (Figure 2c–e). Remarkably, homogeneous and pinhole-free perovskite films with large grain size (~500 nm) are generated at annealing temperatures of 130 and 150 °C (Figure 2d and e). The changes in the morphology reveal that increasing the annealing temperature favors the formation of compact and large-grain perovskite film. X-ray diffraction (XRD) spectra shown in Figure 2f clearly reveal the good crystallinity of the as-prepared perovskite films. The strong diffraction peaks of 14.0°, 20.1°, 28.4°, and 31.7°, attributed to the (110), (200), (220), and (310) lattice planes of the orthorhombic perovskite, respectively, can be clearly observed in all of the perovskite films. The diffraction peak of PbI_2 at 12.56° is only observed in perovskite film at the annealing temperature of 150 °C, indicating the partial decomposition of the perovskite film to PbI_2 at 150 °C.

The compact homogeneous and gain-size-suitable perovskite films result from the use of the mixed NPASs in the film prepared by a one-step solution deposition method. In the one-step solution deposition method, introducing an NPAS is an effective and facile method to obtain uniform and dense perovskite films with large grain size, which promote the rapid formation of perovskite grains by removing the residual solvent in the perovskite precursor solution. We improved the method by introducing mixed NPASs, which are proved to be more effective in removing the residual solvent and favor the formation of compact homogeneous perovskite films with suitable grain size (Supporting Information Figure S2). The perovskite film with pure diethyl ether shows a compact smooth surface and a small grain size. When adding a certain ratio of chlorobenzene, the grain size turns large, while the surface shows rough-borders or rings. In the case of pure chlorobenzene, the grain size is about 1 μm but the film is not very dense.

Hence, the densification and grain size of perovskite film should be properly adjusted and balanced for optimum performance. The optimized mixed NPASs include diethyl ether and chlorobenzene, with volume ratio of 4:1, enabling the formation of the compact homogenous perovskite film with the highest absorption intensity (Supporting Information Figure S3).

The as-prepared perovskite films are utilized to fabricate ESL-free heterojunction PSCs. The schematic device structure is shown in **Figure 3**a, which consists of FTO/perovskite/HTM (spiro-MeOTAD)/Au. The representative photocurrent density–voltage (J–V) curves of the ESL-free PSCs, based on the perovskite films with different annealing temperatures, are shown in Figure 3b. The photovoltaic parameters of the PSCs, including the short circuit current density (J_{SC}), the fill factor (FF), the open circuit voltage (V_{OC}), and the power conversion efficiency (PCE), are summarized in **Table 1**. With increasing annealing temperature from none to 130 °C, corresponding to the change of the perovskite from p- to n-type, the J_{SC} and FF of the PSCs are significantly increased, leading to the impressive increase in the PCE from 3.89 to 14.56%. Moreover, the V_{OC} also increases from 0.95 to 1.04 V with increasing annealing temperature of the perovskite, which can be ascribed to the enhanced n-type doping property of the perovskite and consequently an enhanced electric field in the heterojunction. The device performance is lowered by further increasing the annealing temperature to 150 °C, and by the partial decomposition of the perovskite to PbI_2, which increases the resistance and the carrier recombination in perovskite film.

From the J–V characteristics, it can be seen that the n-type self-doped perovskite exhibits better device performance, which can be well explained by the device working principle of the ESL-free PSCs based on n-type doped perovskite. Figure 3c shows the schematic energy level diagram and the working principle of the PSCs. Photons are absorbed by the perovskite and the free carriers (electrons and holes) are generated in the perovskite film. An electric field can be established in the n-type doped perovskite, which drives the electrons to the cathode, and the holes to the HTM followed by their transportation to the Au anode through the HTM. Hence, both electron and hole selection are efficient in the PSCs with the n-type doped perovskite, enabling their high device performance. For p-type or intrinsic perovskite, both electrons and holes can diffuse to the cathode, and recombine at perovskite/cathode interface, leading to their low device efficiency. Moreover, as the Fermi level of the perovskite can be varied by thermal annealing, the built-in potential across the heterojunction and the V_{OC} of the PSCs can also be optimized. Therefore, with enhanced n-type doped perovskite film (high annealing temperature), the V_{OC} is increased consistently.

Moreover, to investigate the effect of self-doping property of the perovskite films on carrier extraction dynamics in PSCs, time-resolved photoluminescence (TRPL) decays are employed. TRPL decay profiles for perovskites with different doping types (**Figure 4**) varies with the doping type, as their lifetime first decreases with perovskite changing from p-type (none annealing) to lightly n-type doped (annealing at 100 °C), and then increases with the perovskite becoming n-doped (annealing at 150 °C). This similar trend has been reported in our previous work,[22] which can be explained by the recombination
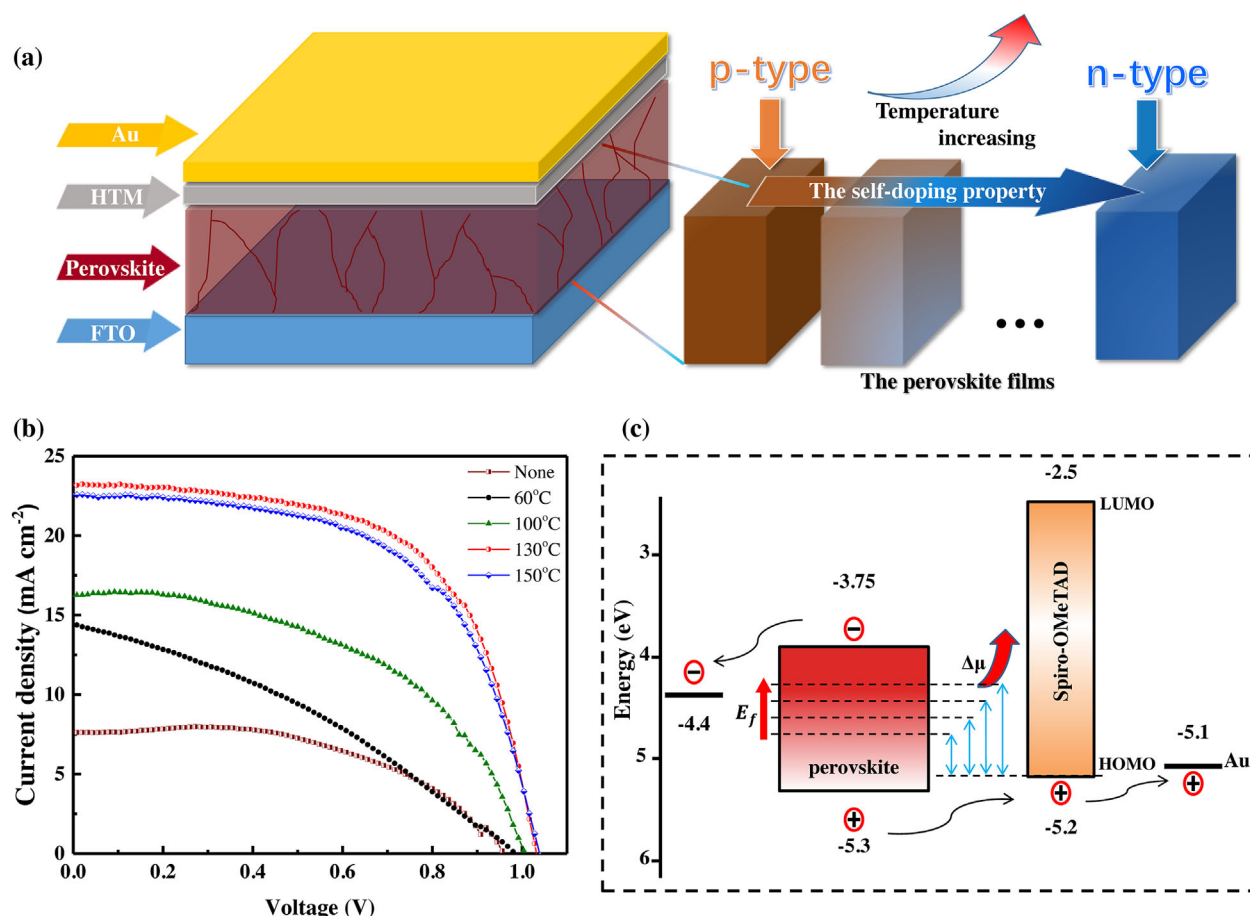
Figure 3. (a) Device architecture of the perovskite solar cells without electron-selective layer and schematic illustration of the change in self-doping property of the perovskite film. (b) J–V curves of electron-selective layer-free perovskite solar cells with different perovskite annealing temperatures. (c) Energy level diagram of the electron-selective layer-free perovskite solar cells.

mechanism inducing the PL decay in the perovskite films. With depositing (spiro-MeOTAD) on the perovskite film, hole extraction occurs at perovskite/HTM interface, leading to the accelerated decay in PL intensity. As shown in Figure 4, the HTM shows a stronger quenching effect (better hole extraction) on the n-type perovskite film than on the p-type doped perovskite film, revealing the establishment of the perovskite/HTM hetero-junction with n-doped perovskite for enhanced hole extraction at perovskite/HTM interface. The enhanced hole extraction reduces the carrier recombination at the perovskite/HTM
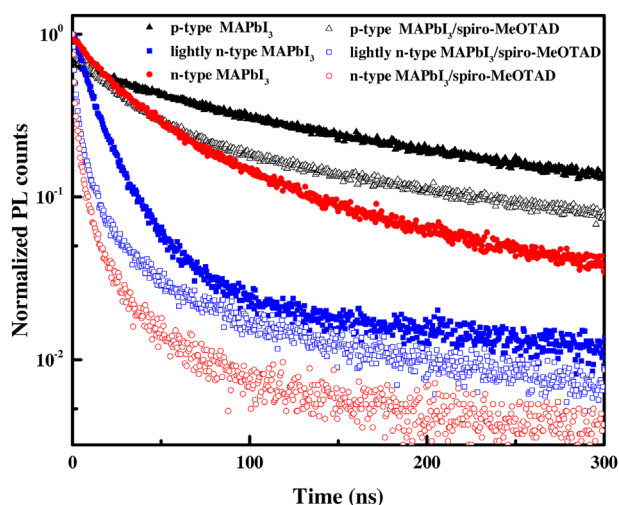
interface and inside the perovskite film, leading to the improved photovoltaic performance of the ESL-free heterojunction PSCs with n-type perovskite.

The efficiency distribution of the PSCs with perovskite film annealed at 130 °C and using the mixed NPASs ratio of 4:1 vol between diethyl ether and chlorobenzene is shown in Supporting Information Figure S4. The parameters are obtained from 65 individual devices fabricated with the same process. The V_{OC} values are highly reproducible and in excess of 1.0 V, and the average J_{SC} values are around 21 mA cm^{-2}. The FF values are generally higher than 55%, which exceed other reports in this architecture,[15–17] leading to an average PCE of 13.2%. Hence, the ESL-free heterojunction PSCs with n-type doped perovskite present stable reproducibility and high device performance.

The highest efficiency achieved by the ESL-free PSCs is 15.69% (as shown in **Figure 5**a). The high PCE of 15.69% makes this PSC one of the highest performing ESL-free PSCs reported to date. It is also worth noting that the high efficiency of 15.69% of the as-fabricated ESL-free heterojunction PSCs is obtained utilizing all-solution processes without any extremely high temperature processing, which is beneficial for the commercial-ization of the PSCs. Figure 5a inset presents the external quantum efficiency (EQE) spectrum of the ESL-free

Table 1. Photovoltaic parameters extracted from J–V curves of electron-selective layer-free perovskite solar cells with different perovskite annealing temperatures.

PSCs	J_{sc} (mA cm^{-2})	FF	V_{oc} (V)	PCE (%)	Max. PCE (%)
None	7.66	0.53	0.95	3.89	4.45
60 °C	14.50	0.33	0.99	4.76	4.93
100 °C	16.26	0.50	1.00	8.24	9.46
130 °C	23.21	0.61	1.03	14.56	15.69
150 °C	22.58	0.58	1.04	13.67	13.87

Figure 4. Time-resolved photoluminescence decay profiles excited by a 485 nm pulse laser and obtained at 760 nm for the FTO/perovskite (MAPbI$_3$)/PolymethylMethacrylate (PMMA) and FTO/MAPbI$_3$/spiro-MeOTAD/PMMA films.

heterojunction PSC, which shows an EQE around or higher than 80% in the full visible light region, indicating the good light and carrier harvesting efficiency in the ESL-free heterojunction PSCs. The integrated J_{SC} is 21.56 mA cm^{-2}, close to the J_{SC} (22.97 mA cm^{-2}) obtained under AM 1.5G solar simulator. ESL-free PSCs also exhibit hysteresis and a weak dependence of the device efficiency on the measurement scanning speeds. The IV-curves measured at varied scanning voltage steps and delay time are shown in Supporting Information Figure S5(a). Meanwhile, the stabilized electric power output and the photocurrent density at maximum power point measured over a period of 200 s are shown in Supporting Information Figure S5(b). By holding a bias near the maximum power output point (0.81 V), we obtained a stabilized PSC of 15%, near the measured PCE of 15.55% for the same cell. Figure 5b shows the cross-sectional image of an

ESL-free PSC composed of stacked layers of FTO/CH$_3$NH$_3$PbI$_3$/spiro-MeOTAD/Au, which highlights the compact large perovskite crystallite ($\sim$400 nm) and excellent homogeneous surface coverage of the perovskite layer on the FTO substrate. Hence, the n-type doped, homogeneous perovskite layer can enable higher performance of the ESL-free PSCs.

The stability features of the PSCs are also investigated. Supporting Information Figure S6 shows the long-term stability of the photovoltaic parameters of the PSCs with and without ESLs. The PSCs were stored in ambient air without encapsulation under dark conditions. The FF and PCE of the ESL-free PSCs first increase and then decrease. The V$_{OC}$ of the ESL-free PSCs remains constant for a long period (21 days). The initial increase in the performance of the ESL-free PSCs may be attributed to the stabilization of the FTO/perovskite interface. The PCE of the non-encapsulated ESL-free PSCs is equally to its initial value after 21 days. In comparison, the standard planar PSC shows a 20% decrease in device efficiency. The FTO/perovskite interface has higher stability than the TiO$_2$/perovskite interface for perovskite films. The oxygen vacancies in TiO$_2$ induce the decomposition of the perovskite film, causing PSCs degradation. Hence, it is clear that the as-fabricated ESL-free heterojunction PSCs possess better long-term stability than the conventional planar PSCs.

Summary: In summary, we have demonstrated a heterojunction concept with n-type self-doped perovskite film for highly efficient ESL-free PSCs. The self-doping property of the perovskite films is controlled by defects engineering, which changes from p- to n-type by increasing the annealing temperature. Meanwhile, compact homogeneous perovskite films with suitable grain size are achieved by the modified one-step solution deposition method. The ESL-free heterojunction PSCs with n-type self-doped and compact homogeneous perovskite films exhibit a high efficiency of 15.69%, which is one of the highest PCE of the ESL-free PSC reported yet, together with superior long-term stability. This work provides an efficient way to construct highly efficient ESL-free PSCs and highlights the great potential of simplifying the PSCs device architecture for further commercialization.
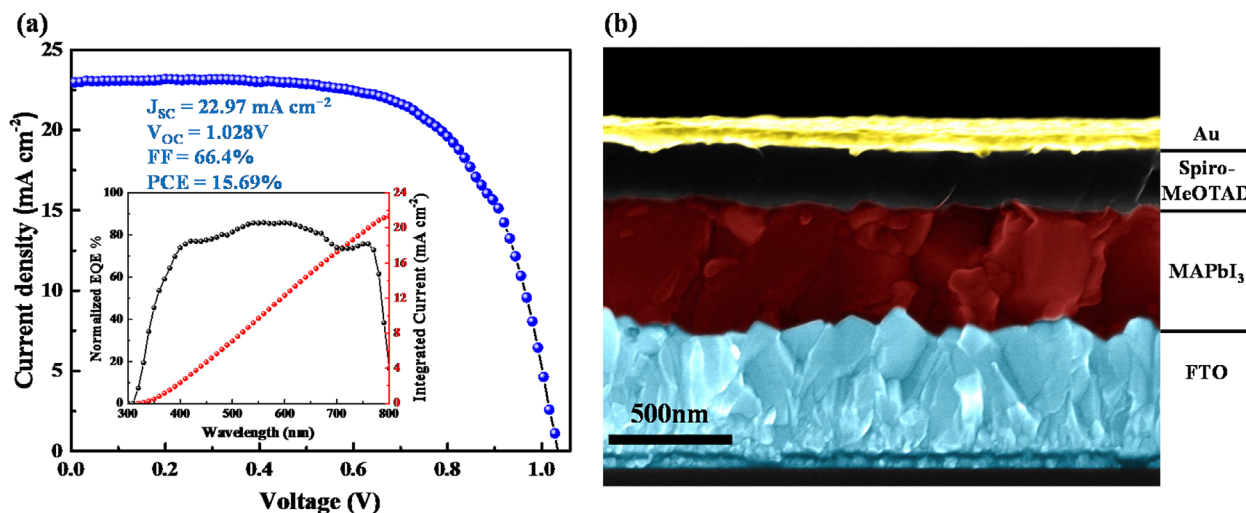
Figure 5. (a) *J–V* curve of the best performed electron-selective layer-free perovskite solar cell, measured under simulated AM 1.5 100 mW cm^{-2} illumination. Inset is its EQE spectrum. (b) Cross-sectional SEM images of ESL-free PSC: FTO/CH$_3$NH$_3$PbI$_3$ layer/spiro-MeOTAD/Au.

ADVANCED
SCIENCE NEWS
www.advancedsciencenews.com

Solar RRL
www.solar-rrl.com

RAPID RESEARCH LETTER

Experimental Section: *Fabrication of CH₃NH₃PbI₃ Films and PSCs*: CH₃NH₃PbI₃ films were fabricated using a modified one-step solution deposition method with consecutive non-polar aprotic solvent (NPAS) dripping. The perovskite precursor solution contained 159 mg MAI, and 461 mg PbI₂ in anhydrous dimethylformamide/dimethylsulphoxide (600 mg/78 mg) solution, which was spin-coated directly on the ultraviolet–ozone treated FTO substrate at 4000 r.p.m. for 30 s. During the spinning step, 0.5 ml of mixed NPASs (diethyl ether/chlorobenzene, ratio of 5:0, 4:1, 3:2, 2:3, 1:4, and 0:5 vol) was slowly poured on the spinning substrate 20 s before the end. The substrates were then annealed at none, 60, 100, 130, and 150 °C, respectively, for 10 min in a nitrogen-filled glove box. For fabricating PSCs, the HTM layer was deposited sequentially and Au electrode was sputtered as reported in our previous work[22,26,27]: after the perovskite annealing, the substrates were cooled down for a few minutes and a spirofluorene-linked methoxy triphenylamines (spiro-MeOTAD) solution (70 mM in chlorobenzene) including tert-butylpyridine and lithium bis (trifluoromethanesulfonyl) imide was spun at 3000 r.p.m. for 30 s. Finally, 80–90 nm of gold top electrode was deposited by magnetron sputtering.

Characterization: Current–voltage curves were measured using a source meter (Keithley 2400) under AM 1.5G irradiation with a power density of 100 mW cm⁻² from a solar simulator (XES-301S+EL-100). The morphologies of the as-prepared CH₃NH₃PbI₃ films were characterized by a scanning electron microscopy (SEM) (Hitachi S-4800). The chemical compositions and structures of the films were analyzed by XRD (Bruker D8 Advance X-ray diffractometer, Cu-K$_\alpha$ radiation $\lambda = 0.15406$ nm). The valence spectra were measured by X-ray photoelectron spectroscopy (XPS) (ESCSLAB 250Xi). All spectra were shifted to account for sample charging using inorganic carbon at 284.80 eV as a reference. Time-resolved photoluminescence (TRPL) decay of the perovskite films on FTO substrates was measured using a transient state spectrophotometer (Edinburgh Ins. F900) under the irradiation of a 485 nm pulse laser. The external quantum efficiency (EQE) was measured using QE-R systems (Enli Tech.). The Hall effect was characterized using a Nanometrics HL5500 Hall System.

Supporting Information: Additional supporting information may be found in the online version of this article at the publisher's website.

Acknowledgements

[1] Kojima, A., Teshima, K., Shirai, Y., Miyasaka, T., *J. Am. Chem. Soc.* **2009**, *131*, 6050.

[2] Im, J. H., Lee, C. R., Lee, J. W., Park, S. W., Park, N. G., *Nanoscale* **2011**, *3*, 4088.

[3] Docampo, P., Hanusch, F., Stranks, S. D., Döblinger, M., Feckl, J. M., Ehrensperger, M., Minar, N. K., Johnston, M. B., Snaith, H. J., Bein, T., *Adv. Energy. Mater.* **2014**, *4*, 1400355.

[4] Wojciechowski, K., Stranks, S. D., Abate, A., Sadoughi, G., Sadhanala, A., Kopidakis, N., Rumbles, G., Li, C., Friend, R. H., Jen, A. K. Y., Snaith, H. J., *Acs Nano* **2014**, *8*, 12701.

[5] Yang, W. S., Noh, J. H., Jeon, N. J., Kim, Y. C., Ryu, S., Seo, J., Seok, S. I., *Science* **2015**, *348*, 1234.

[6] http://www.nrel.gov/ncpv/images/efficiency_chart.jpg.

[7] Bergmann, V.W., Weber, S.A., Javier, R.F., Nazeeruddin, M.K., Grätzel, M., Li, D., Domanski, A.L., Lieberwirth, I., Ahmad, S., Berger, R., *Nat. Commun.* **2014**, *5*, 5001.

[8] Edri, E., Kirmayer, S., Henning, A., Mukhopadhyay, S., Gartsman, K., Rosenwaks, Y., Hodes, G., Cahen, D., *Nano Lett.* **2014**, *14*, 1000.

[9] Kim, H. S., Lee, C. R., Im, J. H., Lee, K. B., Moehl, T., Marchioro, A., Moon, S. J., Humphry-Baker, R., Yum, J. H., Moser, J. E., Grätzel, M., Park, N. G., *Sci. Rep.* **2012**, *2*, 591.

[10] Liu, M., Johnston, M. B., Snaith, H. J., *Nature* **2013**, *501*, 395.

[11] Etgar, L., Gao, P., Xue, Z., Peng, Q., Chandiran, A. K., Liu, B., Nazeeruddin, M. K., Grätzel, M., *J. Am. Chem. Soc.* **2012**, *134*, 17396.

[12] Shi, J., Dong, J., Lv, S., Xu, Y., Zhu, L., Xiao, J., Xu, X., Wu, H., Li, D., Luo, Y., *Appl. Phys. Lett.* **2014**, *104*, 063901.

[13] Tsai, K. W., Chueh, C. C., Williams, S. T., Wenb, T. C., Jen, A. K. Y., *J. Mater. Chem. A* **2015**, *3*, 9128.

[14] Li, Y., Ye, S., Sun, W., Yan, W., Li, Y., Bian, Z., Liu, Z., Wang, S., Huang, C., *J. Mater. Chem. A* **2015**, *3*, 18389.

[15] Liu, D., Yang, J., Kelly, T. L., *J. Amer. Chem. Soc.* **2014**, *136*, 17116.

[16] Ke, W., Fang, G., Wan, J., Tao, H., Liu, Q., Xiong, L., Qin, P., Wang, J., Lei, H., Yang, G., *Nat. Commun.* **2015**, *6*, 6700.

[17] Meng, Y., Fang, G., Wang, J., Tan, F., Nan, L., *ACS Appl. Mater. Inter.* **2015**, *7*, 17592.

[18] Xu, X., Chen, Q., Hong, Z., Zhou, H., Liu, Z., Chang, W. H., Sun, P., Chen, H., Marco, N. D., Wang, M., *Nano Lett.* **2015**, *15*, 6514.

[19] Leijtens, T., Eperon, G. E., Pathak, S., Abate, A., Lee, M. M., Snaith, H. J., *Nat. Commun.* **2013**, *4*, 94.

[20] Wang, Q., Shao, Y., Xie, H., Lyu, L., Liu, X., Gao, Y., Huang, J., *Appl. Phys. Lett.* **2014**, *105*, 163508.

[21] Yin, W. J., Shi, T., Yan, Y., *Appl. Phys. Lett.* **2014**, *104*, 063903.

[22] Song, D., Cui, P., Wang, T., Wei, D., Li, M., Cao, F., Yue, X., Fu, P., Li, Y., He, Y., *J. Phys. Chem. C* **2015**, *26*, 22812.

[23] Ahn, N., Son, D. Y., Jang, I. H., Kang, S. M., Choi, M., Park, N. G., *J. Am. Chem. Soc.* **2015**, *137*, 8696.

[24] Jeon, N. J., Noh, J. H., Kim, Y. C., Yang, W. S., Ryu, S., Seok, S. I., *Nat. Mater.* **2014**, *13*, 897.

[25] Xiao, M., Huang, F., Huang, W., Dkhissi, Y., Zhu, Y., Etheridge, D. J., Gray-Weale, A., Bach, D. U., Cheng, D. Y. B., Spiccia, D. L., *Angew. Chem.* **2014**, *53*, 9898.

[26] Song, D., Wei, D., Cui, P., Li, M., Duan, Z., Wang, T., Ji, J., Li, Y., Mbengue, J. M., Li, Y., He, Y., Trevora, M., Park, N. G., *J. Mater. Chem. A* **2016**, *4*, 6091.

[27] Wei, D., Wang, T., Ji, J., Li, M., Cui, P., Li, Y. Y., Li, G., Mbengue, J. M., Song, D., *J. Mater. Chem. A* **2016**, *4*,1991.

[28] Guerrero, A., Juarezperez, E. J., Bisquert, J., Morasero, I., Garciabelmonte, G., *Appl. Phys. Lett* **2014**, *105*, 133902.

[29] Jiang, C. S., Yang, M., Zhou, Y., To, B., Nanayakkara, S. U., Luther, J. M., Zhou, W., Berry, J. J., de Lagemaat, J. v., Padture, N. P., Zhu, K., Al-Jassim, M. M., *Nat. Commun.* **2015**, *6*, 8397.